ORIGINAL ARTICLE

Astronomische
Nachrichten

Neutron star collisions and gravitational waves

Matthias Hanauske[1,2] | Lukas R. Weih[1]

[1]Department for Theoretical Physics, Institut für Theoretische Physik, Goethe Universität, Frankfurt, Germany

[2]Department for Theoretical Physics, Frankfurt Institute for Advanced Studies, Frankfurt, Germany

Correspondence

Matthias Hanauske, Institut für Theoretische Physik, Max-von-Laue-Straße 1, 60438 Frankfurt, Germany.
Email: hanauske@th.physik.uni-frankfurt.de

Abstract

The long-awaited detection of a gravitational wave from the merger of a binary neutron star in August 2017 (GW170817) marked the beginning of the new field of multi-messenger gravitational wave astronomy. By exploiting the extracted tidal deformations of the two neutron stars from the late inspiral phase of GW170817, it was possible to constrain several global properties of the equation of state of neutron star matter. By means of fully general-relativistic hydro-dynamic simulations, it is possible to get an insight into the hydrodynamic evolution of matter and into the structure of the space–time deformation caused by the remnant of binary neutron star merger. Neutron star mergers represent an optimal astrophysical laboratory to investigate the phase transition from confined hadronic matter to deconfined quark matter. With future gravitational wave detectors, it will most likely be possible in the near future to investigate the hadron-quark phase transition by analyzing the spectrum of the post-merger gravitational wave of the differentially rotating hypermassive hybrid star. In contrast to hypermassive neutron stars, these highly differentially rotating objects contain deconfined strange quark matter in their slowly rotating inner region.

KEYWORDS

Einstein's equations, general relativity, gravitational waves, neutron star collisions

1 | THE NEW WAY OF LOOKING AT OUR UNIVERSE

For a long time, the study of astrophysical processes was limited to events visible with the eyes, and optical telescopes did not develop until the 16th century. The perception of the universe in the other frequency bands of the electromagnetic radiation was made possible by radio, infrared, and X-ray telescopes, which were only built in the 20th century. The entire perceived image that we had of our universe was therefore limited to astrophysical phenomena that generate electromagnetic radiation. This

circumstance changed in the 21st century with the detection of gravitational waves. It is as if humanity has new miraculous glasses, like a new sensory organ, with which it can detect previously unobservable processes in our universe.

On September 14, 2015, almost exactly a hundred years after Albert Einstein developed the field equations of general relativity (Einstein 1915a, 1915b) and predicted the existence of gravitational waves (Einstein 1918) these curious spacetime-ripples have been observed from a pair of merging black holes by the LIGO detectors (GW150914, The LIGO Scientific Collaboration & the

Virgo Collaboration 2016). In the following years, three scientific observable runs were carried out, with the results of the first two fully evaluated and published The LIGO Scientific Collaboration and the Virgo Collaboration (2019a). By means of the gravitational-wave detectors LIGO and Virgo, 11 gravitational waves have be detected within the first two observing runs, whereby one of these gravitational waves (GW170817) was caused by the collision of two neutron stars (Abbott, Abbott, Abbott, Acernese et al. 2017, Abbott, Abbott, Abbott et al. 2017) about 130 million years ago. Electromagnetic radiation in all frequency ranges was also detected during this event (Abbott, Abbott, Abbott, Acernese et al. 2017, Abbott, Abbott, Abbott et al. 2017; Troja et al. 2017) and an emitted gamma-ray burst (GRB 170817A, LIGO Scientific Collaboration, Virgo Collaboration, Gamma-Ray Burst Monitor, & INTEGRAL 2017) hit the gamma-ray satellite telescopes with a delay of 1.7 s. Space-based gamma-ray telescopes (e.g., the Fermi's gamma-ray burst monitor or the Swift gamma-ray burst mission) detect on average approximately one gamma-ray burst per day—however, the gamma-ray burst (LIGO Scientific Collaboration et al. 2017) that had been associated with GW170817 is an outstanding event and, in addition, with the observations of the electromagnetic counterparts of the associated kilonova, provides a conclusive picture of the whole merger event. This coincidence of the direct detection of a gravitational wave from a neutron star collision with the emitted short gamma-ray burst was the first observational proof that binary neutron star mergers generate short gamma-ray bursts.

The gravitational waves observed by LIGO and Virgo between April 2019 and October 2019, within the third observing run, are still only partly analyzed and during the first half of this observational period 39 candidates of gravitational wave events were found and four of these have already been analyzed and were published (The LIGO Scientific Collaboration & the Virgo Collaboration 2020d). GW190425 (The LIGO Scientific Collaboration & the Virgo Collaboration 2020a) the second gravitational wave event of a binary neutron star merger, had a significantly larger total mass $m_{tot} \approx 3.4 M_\odot$ than GW170817 ($m_{tot} \approx 3.4 M_\odot$) and far exceeds the masses of Galactic double neutron stars known through radio astronomy. GW190814 (The LIGO Scientific Collaboration & the Virgo Collaboration 2020c) is an extremely asymmetrical system having a 23 black hole merging with a $\approx 2.6 M_\odot$ object, which either is the lightest black hole or heaviest neutron star known to be in a double compact object system. GW190521 (The LIGO Scientific Collaboration & the Virgo Collaboration 2020b, 2020e) is merger of two black holes with masses of $85^{+21}_{-14} M_\odot$ and $66^{+17}_{-18} M_\odot$ ($m_{tot} \approx 150 M_\odot$), where the primary black hole mass lies within the gap produced by pair-instability supernova processes and the mass of the produced remnant black hole ($142^{+28}_{-16} M_\odot$) can be considered an intermediate mass black hole.

Additionally, the detections imply that gravitational waves travel at the speed of light, with deviations smaller than a few 10^{-15} and the detected gravitational wave forms in combination with the information from the observed electromagnetic counterpart of GW170817 constrain the equation of state, alternative theories of gravity, possible effects due to large extra dimensions, and dark energy models (Copeland et al. 2019; Creminelli & Vernizzi 2017; The LIGO Scientific Collaboration & the Virgo Collaboration 2019b). Furthermore, constraints on cosmic strings (The LIGO Scientific Collaboration, the Virgo Collaboration, & the KAGRA Collaboration 2021a) and upper limits on continuous gravitational-wave signals from the young pulsar PSR J0537-6910 (The LIGO Scientific Collaboration, the Virgo Collaboration, & the KAGRA Collaboration 2020) and on the isotropic gravitational-wave background (The LIGO Scientific Collaboration, the Virgo Collaboration, & the KAGRA Collaboration 2021b) could be specified.

2 | EINSTEIN'S THEORY OF SPACE–TIME CURVATURE

Albert Einstein presented his revolutionary Theory of General Relativity to the scientific public in the year 1915 (Einstein 1915a, 1915b). He derived his field equations by means of a general principle of covariance, and in the (Einstein 1915a) research paper he wrote about his theory: "Hardly anyone who has really grasped the theory will be able to escape the magic of it; … "[1] As early as 1914 he wrote: "In particular, I succeeded in obtaining the equations of the gravitational field in a purely covariant theoretical way." (Einstein 1914). The beauty of the Einstein equation, along with its underlying principle of covariance, lies in the simplicity of its fundamental statement. According to Einstein, every accumulation of energy bends the structure of space–time and this curved space–time is the causal reason of gravity. According to Einstein, the apple falls from the tree to the ground, because the earth's great energy content bends the space–time structure so much that the apple has to move to the ground in this curved spacetime according to geodetic laws.

Einstein's theory of general relativity in connection with the conservation laws for energy-momentum and rest mass are the groundings of neutron star collisions

---

[1] "Dem Zauber der Theorie wird sich kaum jemand entziehen können, der sie wirklich erfasst hat; … "

and gravitational waves. The Einstein equation and the conservation laws are summarized in the following set of highly non-linear differential equations:

$$R_{\mu\nu} - \frac{1}{2}g_{\mu\nu}R = 8\pi\,T_{\mu\nu}, \quad \nabla_\mu T^{\mu\nu} = 0, \quad \nabla_\mu(\rho u^\mu) = 0, \quad (1)$$

where $T_{\mu\nu}$ is the energy-momentum tensor, $R_{\mu\nu}$ is the Ricci tensor, which contains first and second derivatives of the space–time metric $g_{\mu\nu}$, ∇_μ is the covariant derivative, and u^μ is the four velocity of the underlying matter. The Einstein equation (first equation in Equation 1) describes in which way the space–time structure needs to bend (left hand side of the equation) if energy-momentum is present (right hand side of the equation).

It did not take long to find the first stationary solution to the Einstein equations. Just a few months after Einstein's article was published, Karl Schwarzschild worked out two possible analytical solutions to the new theory of space–time curvature (Schwarzschild 1916a, 1916b). In the first of these works ("On the gravitational field of a mass point according to Einstein's theory"), Mr Schwarzschild considered the Einstein equation for free space ($T_{\mu\nu} \equiv 0$), with the restriction on a time-independent and spherically symmetric metric. The solution of the resulting field equations is now known as the "Schwarzschild solution" and is: $g_{\mu\nu} = \mathrm{diag}(-(1 - 2M/r), (1 - 2M/r)^{-1}, r^2, r^2\sin^2(\theta))$, where $x^\mu = (t, r, \theta, \phi)$ and M is the gravitational mass of the mass point. This solution is of particular importance for astrophysical considerations because it describes on the one hand the metric of a non-rotating black hole and on the other hand, based on the Birkhoff theorem (Birkhoff 1923; Jebsen 1921), the metric outside of a single isolated, non-rotating star.[2] In order to calculate the space–time structure within a spherically symmetrical body, one has to consider the entire Einstein equation ($T_{\mu\nu} \neq 0$) and the solution depends on the equation of state of matter within the object. Assuming that the body consists of an static ideal fluid ($T_{\mu\nu} = (e + p)u_\mu u_\nu + p\,g_{\mu\nu}$, where e is the energy density and p the pressure), Tolman, Oppenheimer, and Volkoff were able to show in 1939 how the inner solution can be calculated and connected to the outer Schwarzschild solution (Oppenheimer & Volkoff 1939; Tolman 1939).

In the last paragraph, some of the fundamental static solutions of the Einstein equation are listed. However, to simulate the evolution of a binary neutron star system, including the neutron star collision and gravitational wave emission process, we need to reformulate the equation in Equation (1) in order to solve the time-dependent problem

numerically. This reformulation, the so called (3 + 1)-split, starts by slicing the four-dimensional manifold $\mathcal{M}$ into three-dimensional space-like hypersurfaces Σ_t. The space–time metric $g_{\mu\nu}$ is then also divided into a purely spatial metric γ_{ij}, a lapse function α and a shift vector β_i:

$$g_{\mu\nu} = \begin{pmatrix} -\alpha^2 + \beta_i\beta^i & \beta_i \\ \beta_i & \gamma_{ij} \end{pmatrix}, \quad \mu = t, x, y, z; i = x, y, z \quad (2)$$

The lapse function α describes the difference between the coordinate time t and the proper time of a fluid particle τ ($d\tau = \alpha\,dt$). The shift vector β_i measures how the coordinates are shifted on the spatial slice if the fluid particle moves an infinitesimal time step further. By inserting the metric (Equation 2) into the Einstein equation, one can reformulate the equations into a system of first-order differential equations, the so called ADM equations (Arnowitt et al. 1959) (named for its authors Richard Arnowitt, Stanley Deser and Charles W. Misner). As the ADM equations are not "well posed" and contain weakly hyperbolic parts, the equations need to be further transformed, by using conformal traceless metric transformation (for details see Rezzolla & Zanotti 2013). These formulation of general relativity (e.g. BSSNOK, CCZ4) together with the relativistic hydrodynamic equations (within the "Valencia" formulation, Martí et al. 1991) are finally used as the grounding equations in many contemporary computer programs.

The simulations, which will be presented in the following, are performed within the `Einstein Toolkit` Löffler et al. (2012) together with the `WhiskyTHC` (Radice et al. 2014a, 2014b) code using the conformal and covariant CCZ4 formulation (for details see Weih et al. 2020). On the initial space-like hypersurfaces Σ_{In} an irrotational binary neutron star configuration in a circular orbit was placed using an initial separation of 45 km. Due to the emission of gravitational waves, the distance between the two neutron stars decreases with time and Figure 1 depicts the main hydrodynamical and space–time properties of the system a few orbital circles later.

In the upper plane, the rest mass density ρ in the equatorial plane is shown. In order to adequately illustrate the different density zones, two color scales have been used: a linear density scale in units of the normal nuclear matter density ($\rho_0 = 2.705 * 10^{14}$ g/cm^3) which represents the high-density region $\rho \in [0.1, 5.2]\,\rho_0$ and a logarithmic density scale which illustrates the outer crust and low-density region. At this time in the inspiral phase ($t = -5.4$ ms, relative to the time of the merger), the two neutron stars are still largely not deformed and only deviate slightly from the TOV solutions of two separated neutron stars.

The plane in the middle shows the main contribution of space–time bending to the g_{tt}-component of the metric,

---

[2]The stationary and axially symmetric vacuum solution of Einstein's field equations, which describes the space–time structure of rotating black holes was found in the year 1963 by Roy Kerr (1963).
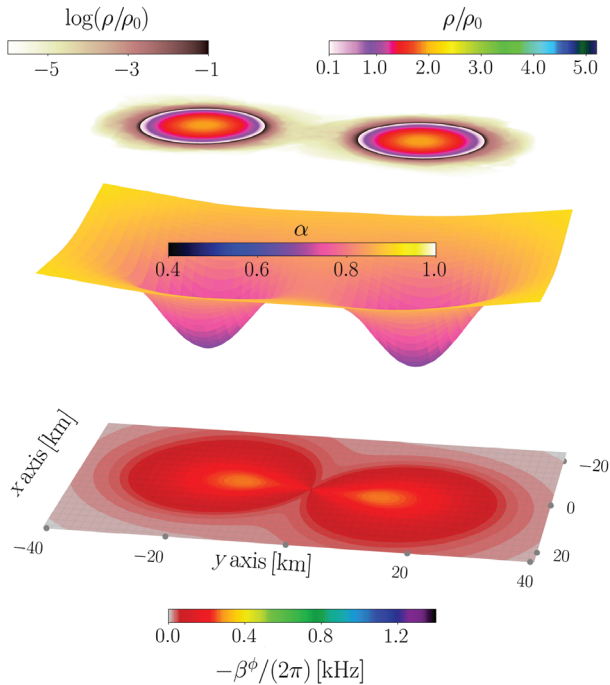
FIGURE 1   Hydrodynamic properties of matter and space–time during the inspiral phase of a neutron star merger

namely, the lapse function α. Due to the large neutron star masses (equal-mass binary with $M = 1.32 M_\odot$ for each star) and central densities ($\rho_{max} = 1.95 \rho_0$) the space–time structure is deformed within the interior of the stars ($\alpha_{min} = 0.66$) and this inner metric is steadily flowing into the outer metric.[3]

In the lower plane, the frame dragging of space–time is visualized by showing the ϕ-component of the shift vector β^ϕ in kHz

$$\beta^\phi = \frac{x\beta^y - y\beta^x}{x^2 + y^2 + z^2}. \tag{3}$$

The two neutron stars rotate with a large speed counter clockwise around each other and as a consequence the space–time structure follows the movement of the large accumulation of energy.

3 | ASTROPHYSICAL CONSTRAINTS OF THE EQUATION OF STATE OF ELEMENTARY MATTER

Neutron star mergers are in general a complicated interplay between all known forces, however, two elementary forces dominate the system, namely, the strongest

(quantum chromo dynamics, QCD) and the weakest forces (gravity described by general relativity). Unfortunately, QCD is not solvable in the nonperturbative regime and, up to now, numerical solutions of QCD on a finite space–time lattice are still unable to describe neutron star matter or even finite nuclei or infinite nuclear matter. As a consequence, several effective theoretical models of the hadronic interaction have been constructed, however, within the ultra-high density/temperature region, it is believed that hadronic matter undergoes a phase transition to a deconfined state consisting of quarks and gluons, the so-called quark-gluon plasma. High-energy heavy-ion collision data are compatible with a hadron to quark phase transition (HQPT) and during the last decades several experiments have presented results, indicating that such a transition indeed occurs in high-energy nuclear collisions (Aamodt 2010a, 2010b, 2011; Adams 2005; Adcox 2005; Arsene 2005; Gazdzicki 2004; Gazdzicki & Gorenstein 1999). Several astrophysical signatures of the HQPT in the interior of a compact star have been proposed within the last decades and different mass and radius properties (Hanauske 2003; Hanauske & Greiner 2001; Mishustin et al. 2003) and rotational behaviors (Banik et al. 2005; Banik et al. 2004; Bhattacharyya et al. 2005; Glendenning et al. 1997) have been theoretically predicted. The effects of a strong HQPT have been investigated in the context of static (Hanauske & Greiner 2001; Mishustin et al. 2003; Shovkovy et al. 2003) and uniformly rotating hybrid stars (Banik et al. 2004; Bhattacharyya et al. 2005; Glendenning et al. 1997) and the results show that tremendous changes in the star properties might occur including the existence of a third family of compact stars—the so-called "twin stars" (Alford & Sedrakian 2017; Glendenning & Kettner 2000; Hanauske & Greiner 2001; Mishustin et al. 2003).

In addition to high-energy experiments, the equation of state of matter can also be constrained by means of astrophysical observations. By means of radio observations of binary pulsar systems, the mass of some very massive neutron stars could be determined relatively precisely (Antoniadis et al. 2013; Cromartie et al. 2020; Demorest et al. 2010) (e.g. $M = 2.14^{0.10}_{-0.09} M_\odot$ for the millisecond pulsar PSR J0740+6620 Cromartie et al. 2020) and, due to this, models of the equation of state that predict a lower maximum mass could be excluded. By analyzing the soft X-ray pulse waveforms of pulsars observed using the Neutron Star Interior Composition Explorer (NICER) the neutron radius, and as a result the EOS, could be severely constrained (Bilous et al. 2019; Miller et al. 2020; Miller et al. 2019; Raaijmakers et al. 2019; Riley et al. 2019 (e.g. $R = 13.02^{1.24}_{-1.06}$ km for the millisecond pulsar PSR J0030+0451 Miller et al. 2019).

---

[3]Strictly speaking, the concept of an external space–time metric does not exist in numerical relativity, since the entire space is filled with a low density atmospheric fluid.

Since the new era of gravitational wave physics, it is now also possible to constrain the EOS by means of the detected gravitational wave of a neutron star collision. With the use of the observed tidal deformations of the two neutron stars from the late inspiral phase and other properties of GW170817, the EOS of dense matter could be severely constrained (Abbott et al. 2019; Christian et al. 2019; Kiuchi et al. 2019; Paschalidis et al. 2018; Radice et al. 2018; The LIGO Scientific Collaboration & the Virgo Collaboration 2018). New constraints on neutron star radii have been found (Annala et al. 2018; Bauswein et al. 2017; Burgio et al. 2018; De et al. 2018; Malik et al. 2018; Most et al. 2018; Raithel et al. 2018; Tews et al. 2018; The LIGO Scientific Collaboration & the Virgo Collaboration 2018) that are in accordance with the observations from NICER. An upper bound for the maximum mass of neutron stars was estimated (Margalit & Metzger 2017; Rezzolla et al. 2018; Ruiz et al. 2018; Shibata et al. 2019) and the global properties of the HQPT using hybrid star EOSs could be constrained (Annala et al. 2020; Blaschke et al. 2020; Christian & Schaffner-Bielich 2020; Li et al. 2020; Montaña et al. 2019).

All of these articles were only made possible by the measured tidal deformations of the two neutron stars imprinted in the gravitational wave GW170817 emitted during the late inspiral phase. Figure 2 depicts the simulation results during the late inspiral phase at $t = -0.61$ ms, relative to the time of the collision. Although the density profiles, the structure of the lapse function and the frame dragging shift vector still show two separated objects, the tidal density deformations of the two neutron stars can be clearly seen in the upper panel.

The tidal deformability λ quantifies the induced quadrupole moment of a star in response to the quadrupolar tidal gravitational field of the companion in a binary system (Hinderer 2008, 2010), and it can be obtained from the dimensionless $l = 2$ tidal Love number k_2 as

$$k_2 = \frac{3}{2}\lambda R^{-5}, \qquad (4)$$

where R is the radius of the star. The tidal Love number k_2 can be calculated numerically by solving a differential equation together with the TOV equations (see e.g. Postnikov et al. 2010 for details). The dimensionless tidal deformability Λ can then be determined by the equation

$$\Lambda = \frac{2k_2}{3C^5}, \qquad (5)$$

where C is the compactness of the star ($C = M/R$). Since for mass ranges of typical neutron stars it can be shown that $k_2 \propto C^{-1}$ Hinderer et al. 2010; Zhao & Lattimer 2018), the following relation applies in summary $\Lambda \propto C^{-6}$. The
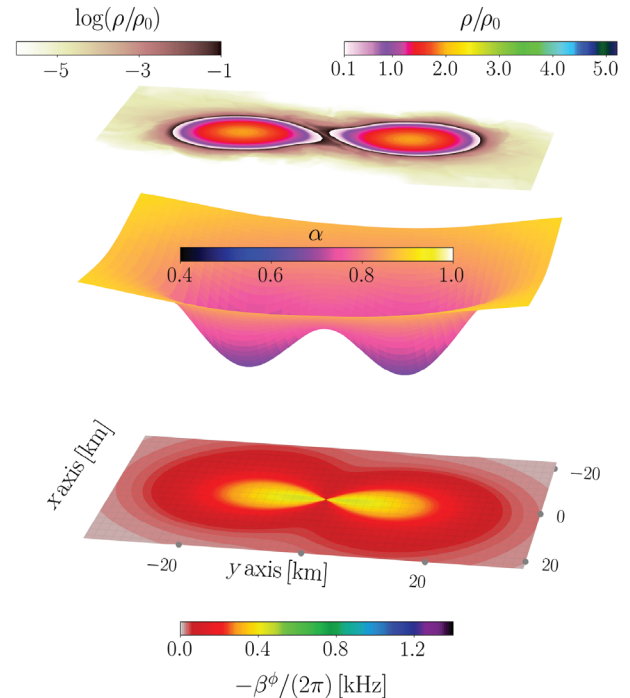
FIGURE 2 Hydrodynamic properties of matter and space–time during the late inspiral phase ($t = -0.61$ ms, see blue circle symbol in Figure 3)

observation of the small value of the tidal deformability in GW170817 therefore corresponds to a large value of the compactness C. This fact, together with the high observed mass values and radius restrictions using the NICER data, ruled out many of the common purely hadronic EOSs, and hybrid EOSs with a strong HQPT became more likely because the phase transition inside these stars enables a higher compactness (Blaschke et al. 2020; Christian & Schaffner-Bielich 2020; Li et al. 2020; Montaña et al. 2019). In future gravitational wave detections of binary neutron star mergers, it might be possible to detect the HQPT, if the phase transition is strong enough. If, for example, the EOS shows a twin star configuration in the mass-radius relation, scenarios can arise in the late inspiral phase in which a purely hadronic star collides with its corresponding hybrid twin and the measured tidal deformability would provide information about the structure of the phase transition (Montaña et al. 2019). Further astrophysical indications of an HQPT, that can occur in the post-merger phase after the collision of the stars, will be discussed in the following.

4 | NEUTRON STAR COLLISIONS

The consequences of an appearance of the HQPT in the interior region of the neutron star merger product and its

impact on the spectral properties of the emitted GWs has been recently discussed in (Bauswein et al. 2019; Blacker et al. 2020; Most et al. 2019; Weih et al. 2020). While in the prompt phase transition scenario (Bauswein et al. 2019; Blacker et al. 2020) a strong first-order phase transition leads, immediately after merger, to the formation of a more compact hybrid star configuration, in the case of a phase-transition-triggered collapse (PTTC) scenario, the phase transition takes place in the post-merger evolution and leads, immediately after its occurrence, to a rapid collapse of the hypermassive hybrid star to a Kerr black hole. In the following, we will discuss in more detail the third possibility of a delayed phase transition (DPT) scenario that was recently presented in Weih et al. (2020).

In the following, we have used for the purely hadronic part of the EOS the relativistic mean-field model FSU2H (Tolos et al. 2017a, 2017b) and added a first-order HQPT including a mixed phase and pure-quark matter region. The soft mixed phase region of this EOS (FSU2H-PT) takes place in the rest-mass density range $\rho/\rho_0 \in [2.085, 4.072]$ and for densities above $4.072\,\rho_0$ a stiff pure-quark matter part was added (for details see Montaña et al. 2019; Weih et al. 2020).

Figure 3 shows the time evolution of the maximum rest-mass density value ρ in units of ρ_0 for the FSU2H-PT (blue and transparent red line) and purely hadronic FSU2H (black line) simulations. In contrast to Weih et al. (2020) (transparent red line, $\Delta x \approx 237\,\text{m}$) we will discuss here the simulation results of a run performed on a somewhat finer grid resolution (blue red line, $\Delta x \approx 189\,\text{m}$). Like in the PTTC case, the phase transition within this DPT scenario takes place at late post-merger times, however, the collapse of the hypermassive neutron star is halted by the formation of a metastable hypermassive hybrid star and the corresponding gravitational wave signatures of a HQPT are more distinct than in the PTTC case.
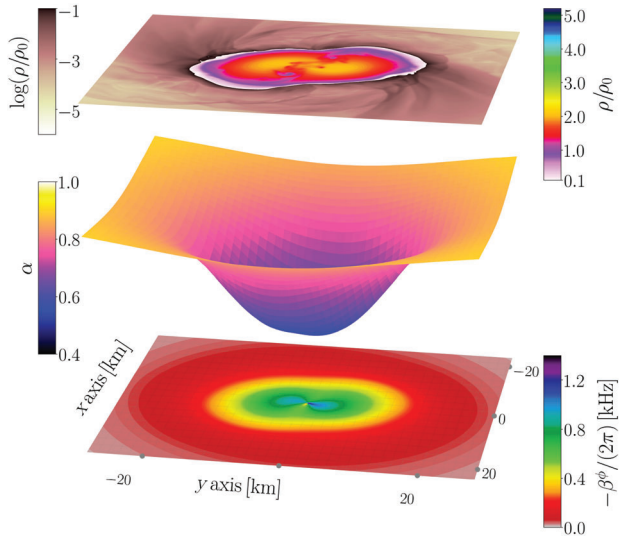
In Figure 2, the density and space–time structure during the late inspiral phase at 0.61 ms before the merger were already shown (see blue circle in Figure 3). Shortly after the merger, the maximum rest-mass density of the remnant increases, reaching a maximum at $t \approx 0.5\,\text{ms}$, that is high enough so that a mixed phase including quark matter is created in the core for both of the FSU2H-PT simulations. The simulation with the higher resolution (blue curve curve) achieves a slightly larger value for the maximum density in comparison to the medium resolution (transparent red curve), since the finer grid is able to better resolve the strong compression of the matter. Next, the density quickly drops and for $t \in [0.5, 2]$ ms the density everywhere in the remnant is again below the onset of the HQPT and no mixed phase matter is present.
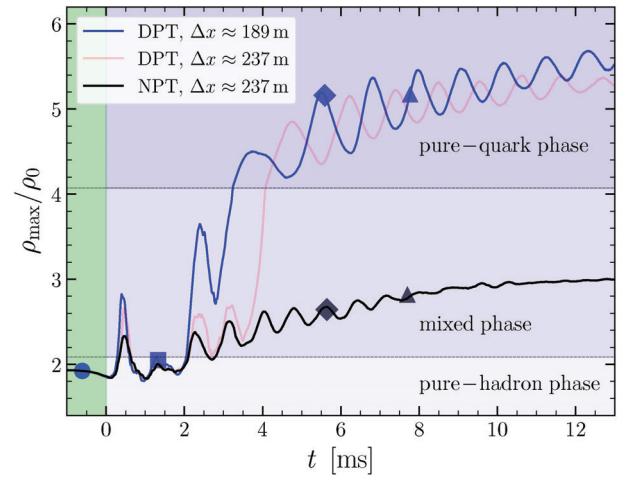
FIGURE 3 Evolution of the maximum rest-mass density for the FSU2H-PT (blue and transparent red line) and FSU2H (black line) simulation with an initial total mass of $M = 2.64 M_\odot$. Symbols mark important times during the evolution that will be discussed in detail in the following

Figure 4 shows the main properties of the hypermassive neutron star at $t = 1.33$ ms. Although the figure shows the simulation results of the FSU2H-PT run, the properties shown also correspond to the results of the FSU2H run, since the short-term hybrid phase within the FSU2H-PT run did not have any major effect on the global dynamics of the star. At this early post-merger phase, the density profile of the remnant (upper panel in Figure 4) shows a pronounced density double-core structure and the frame-dragging rotation of space–time (β^ϕ, lower panel in Figure 4) follows the spatial movement of the high-density regions and also shows a strongly pronounced double-core structure. The structure of the lapse function (α, middle panel in Figure 4), however, no longer shows a double-core structure and a spatial separation of the original individual star components is no longer possible.

Then for $t > 2$ ms the evolution of the FSU2H-PT simulations (blue and transparent red line in Figure 3) starts to differ significantly from the simulation without phase transition (NPT; black line in Figure 3). Figure 3 shows that the impact of the resolution for the two FSU2H-PT simulations does not change the qualitative behavior of the entire evolution of the produced hypermassive hybrid star and the both evolutions of the DPT scenario differs qualitatively from the NPT case. In the high-resolution run (blue line in Figure 3), the collapse of the hypermassive neutron star to the more compact hypermassive hybrid star occurs already at $t \approx 2$ ms with only one intermediate oscillation in the mixed phase, whereas the medium-resolution run shows a somewhat delayed collapse and has two intermediate oscillations in the mixed phase. The DPT occurs in the transient post-merger phase and as a result, the
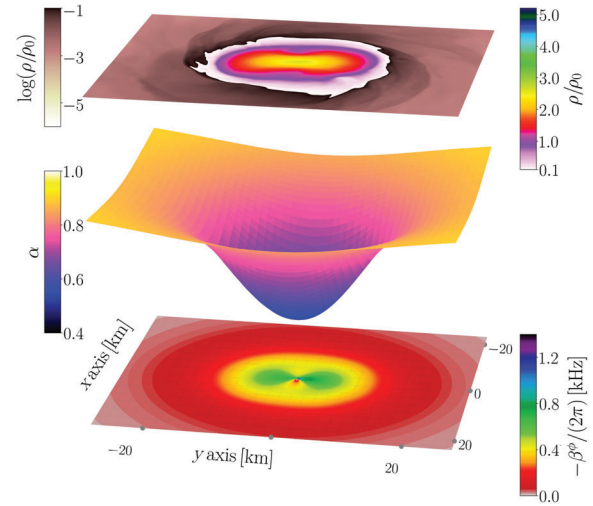
FIGURE 4   Hydrodynamic properties of matter and space–time within the hybrid FSU2H-PT EOS during the post-merger phase at $t = 1.33$ ms (see blue square symbol in Figure 3)
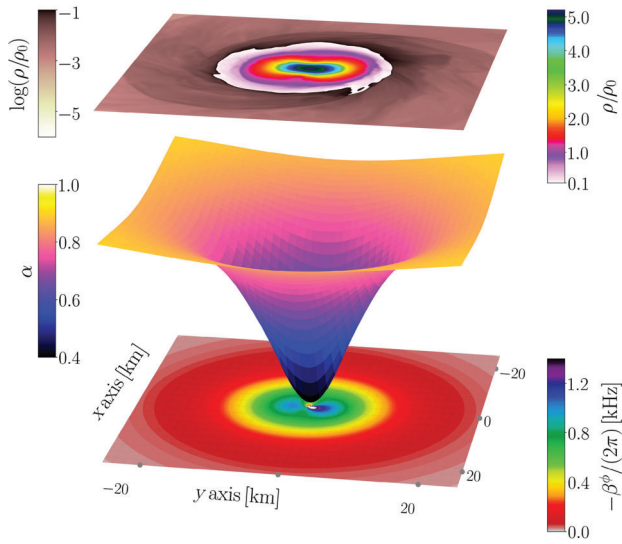

FIGURE 5   Hydrodynamic properties of matter and space–time during the post-merger phase within the purely hadronic FSU2H EOS for $t = 5.64$ ms (see black diamond symbol in Figure 3)

density profile shows a pronounced double-core structure (see Figure 4). At the beginning of the collapse $t \gtrsim 2$ ms, the hypermassive hybrid star still mostly consists of hadronic matter and during the collapse to a smaller and more compact configuration the amount of quark matter in the core significantly increases and the hypermassive hybrid star accelerates its rotation.

Before we analyze the properties and dynamics of the hypermassive hybrid star generated from the DPT collapse, the results of the NPT simulation will be briefly discussed. Figure 5 shows the main properties of the purely hadronic hypermassive neutron star (FSU2H EOS) for $t = 5.64$ ms. The properties of an hypermassive neutron star at such a post-merger time are largely determined by its density profile and its certain differential rotation. The rotating strongly deformed high-density areas of the star (upper panel in Figure 5) tag along with the space–time structure and thereby cause the frame-dragging component β^ϕ shown in the lower panel. Due to the underlying purely hadronic EOS, the star consists mainly of neutrons with small admixtures of hyperons (mainly Λ^0 with some Ξ^-, see Montaña et al. 2019 for details). The maximum central value of the density is $\rho_{max} = 2.60 \rho_0$ and the lapse function α has its minimum value in the center ($\alpha_{min} = 0.53$).

Figure 6, on the contrary, shows the hypermassive hybrid star in the second density maximum after its collapse ($t = 5.59$ ms). The collapse, which was caused by the strong softening of the mixed phase, could be stopped by the emergence of the pure, stiff quark phase. The density in the center of the star ($\rho_{max} = 5.16 \rho_0$) far exceeds the density limit for pure quark matter ($4.072 \rho_0$) of the FSU2H-PT
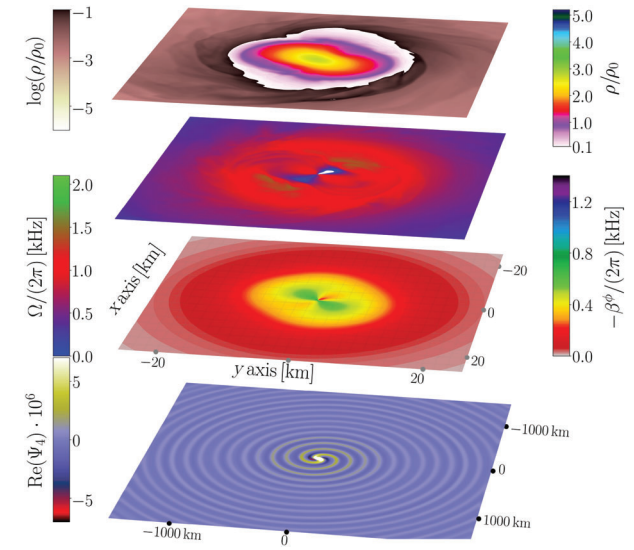
EOS and a large part of the star center consists of deconfined quark matter (upper panel in Figure 6). The small asymmetry in the density profile had been amplified by the collapse, resulting in a large one-sided asymmetry (an $m = 1$ asymmetry in a spherical-harmonics decomposition Baiotti et al. 2007), which triggers a sizeable h_+^{21} gravitational wave strain (see supplemental material of Weih et al. 2020 for details). Due to this density asymmetry, the frame-dragging component β^ϕ (lower panel in Figure 6) shows also a strong one-sided asymmetry. Since the hypermassive hybrid star rotates much faster after the collapse and has a more compact center, it drags space–time with it much more than the purely hadronic hypermassive neutron star. This can be clearly seen from the different colors of the lower panels in Figures 5 and 6. Another major difference is the larger amount of space–time bending of the g_{tt} component of the metric, which is illustrated in the middle panel in Figure 6 by the lapse function and has a minimum value of $\alpha_{min} = 0.38$.

The following evolution of the hypermassive hybrid star is characterized by large density oscillations (see blue and transparent red line in Figure 3 for $t > 5$ ms), during which the density maxima and lapse function minima reached in the center of the are highly correlated. These oscillations are accompanied by a change of the differential rotation profile of the hypermassive hybrid star. At the moment when the rest-mass density reaches its maximum during each oscillation, the hypermassive hybrid star is more compact and spins faster and, as a result, the emitted instantaneous gravitational-wave frequency also reaches a maximum.

The emitted gravitational wave was extracted using the Weyl scalar ψ_4, which is directly related to the metric

FIGURE 6 Hydrodynamic properties of matter and space–time during the post-merger phase within the hybrid FSU2H-PT EOS for $t = 5.59$ ms (see blue diamond symbol in Figure 3)
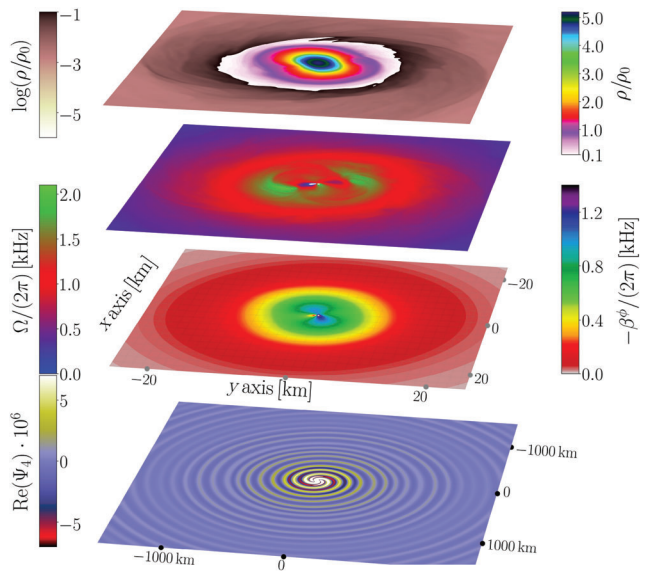
perturbation h_+ and $h_\times$ as follows (for details see Bishop & Rezzolla 2016)

$$\psi_4 = \frac{\partial^2}{\partial t^2}(h_+ - ih_\times). \tag{6}$$

Figure 7 (Figure 8) shows the density ρ, the angular velocity $\Omega = \frac{u^\phi}{u^t} = \alpha v^\phi - \beta^\phi$ (Hanauske, Steinheimer, et al. 2017, Hanauske, Takami, et al. 2017), the shift vector β^ϕ and the real part of the Weyl scalar ψ_4 at a post-merger time of $t \approx 7.7$ ms for the FSU2H simulation (FSU2H-PT high-resolution simulation). In order to exemplify the properties of the emitted gravitational wave (see lower panels) a much larger spatial dimension was chosen than in the three upper panels, that illustrate the internal properties of the remnant. A comparison of the upper panels clearly shows the much more compact density structure of the hypermassive hybrid star (Figure 8). In addition, the panel below shows that it rotates much faster than the hypermassive neutron star (Figure 7, left colored scale in the figures). The qualitative structure of the angular velocity is similar in both remnants and the figures show that the high-density center of the star rotates much slower than the inner middle area. The maxima of the angular velocity are reached at density of $\rho \approx \rho_0$ and the spatial locations of them are closely connected with temperature hot-spots (see Alford et al. 2018; Hanauske, Bovard, et al. 2019; Hanauske, Steinheimer, et al. 2019 for details). A comparison of the third panels from the top show that the frame-dragging component β^ϕ of the hypermassive hybrid star shows a much stronger one-sided asymmetry

FIGURE 7 Hydrodynamic properties of matter and space–time during the post-merger phase within the purely hadronic FSU2H EOS for $t = 7.7$ ms (see black triangle symbol in Figure 3)

FIGURE 8 Hydrodynamic properties of matter and space–time during the post-merger phase within the hybrid FSU2H-PT EOS for $t = 7.77$ ms (see blue triangle symbol in Figure 3)

and in general the frame-dragging is much more pronounced

All these numerically obtained simulation results, although interesting, are not directly observable and can only be detected indirectly by means of a detection of a gravitational wave emitted during the post-merger phase of a neutron star collision, which might be possible in the future. In Hanauske et al. (Hanauske, Steinheimer, et al. 2017, Hanauske, Takami, et al. 2017) it was shown

that the maximum value of the angular velocity profile correlates with the main gravitational-wave frequency f_2 emitted by the remnant within the post-merger phase. This result can be seen by comparing the lower panels of Figures 7 and 8, where the large frequency difference of the emitted gravitational waves can be seen here with the naked eye. The gravitational wave emitted by the hypermassive neutron star (Figure 7) has a much longer wavelength than the space–time wave emitted by the hypermassive hybrid star (Figure 8). A strong increase of the gravitational wave frequency during the collapse in the post-merger phase can be regarded as an astrophysical indication of an HQPT and would confirm the DPT scenario.

5 | SUMMARY

It was shown that hybrid star merger simulations represent an optimal astrophysical laboratory to investigate the phase structure of QCD and in addition with the observations from heavy-ion collisions will possibly provide a conclusive picture on the QCD phase structure at high density and temperature in the near future (Hanauske, Steinheimer, et al. 2017, Hanauske, Takami, et al. 2017). Astrophysical observables of the HQPT were discussed in the context of the inspiral and post-merger phase, with a main focus on the DPT scenario.

In a similar way to the DPT scenario, the collapse in the PDT scenario is stopped by the formation of a quasi-stable hypermassive hybrid star immediately after merger. In contrast, in the PTTC scenario, the hypermassive hybrid star collapses to a Kerr black hole when the phase transition begins to form and the color degrees of freedom of the pure quark core gets macroscopically confined by the formation of the event horizon, producing a gravitational wave ringdown signal which is different from a purely hadronic one Most et al. 2019. Such a gravitational collapse and the formation of an outermost trapped surface inside the star was already discussed by R. Penrose in 1965 in spherical symmetry (Penrose 1965). The density and temperature structure inside the collapsing hypermassive hybrid star, just before the apparent horizon is formed, is remarkably similar to the image of a swan (see Figure 2 in Most et al. 2020).

REFERENCES

Aamodt, K. 2010a, *(ALICE Collaboration)*, *Phys. Rev. Lett*, *105*, 252301.

Aamodt, K. 2010b, *(ALICE Collaboration)*, *Phys. Rev. Lett*, *105*, 252302.

Aamodt, K. 2011, *(ALICE Collaboration)*, *Phys. Rev. Lett*, *106*, 032301.

Abbott, B. P., Abbott, R., Abbott, T. D., et al. 2017, *Phys. Rev. Lett.*, *119*, 161101.

Abbott, B. P., Abbott, R., Abbott, T. D., et al. 2017, *Astrophys. J. Lett.*, *848*(2), L12.

Abbott, B. P., Abbott, R., Abbott, T. D., et al. 2019, *Phys. Rev. X*, *9*(1), 011001.

Adams, J. 2005, (STAR Collaboration), *Nucl. Phys.*, *A757*, 102.

Adcox, K. 2005, (PHENIX Collaboration), *Nucl. Phys.*, *A757*, 184.

Alford, M., & Sedrakian, A. 2017, *Phys. Rev. Lett.*, *119*, 161104.

Alford, M. G., Bovard, L., Hanauske, M., Rezzolla, L., & Schwenzer, K. 2018, *Phys. Rev. Lett.*, *120*, 041101.

Annala, E., Gorda, T., Kurkela, A., Nättilä, J., & Vuorinen, A. 2020, *Nat. Phys.*, *16*(9), 907.

Annala, E., Gorda, T., Kurkela, A., & Vuorinen, A. 2018, *Phys. Rev. Lett*, *120*(17), 172703.

Antoniadis, J., Freire, P. C. C., Wex, N., et al. 2013, *Science*, *340*, 448.

Arnowitt, R., Deser, S., & Misner, C. W. 1959, *Phys. Rev.*, *116*, 1322.

Arsene, I. 2005, *Nucl. Phys*, *A757*, 1.

Baiotti, L., De Pietri, R., Manca, G. M., & Rezzolla, L. 2007, *Phys. Rev. D*, *75*(4), 044023.

Banik, S., Hanauske, M., & Bandyopadhyay, D. 2005, *J. Phys. G Nucl. Phys.*, *31*, S841.

Banik, S., Hanauske, M., Bandyopadhyay, D., & Greiner, W. 2004, *Phys. Rev. D*, *70*, 123004.

Bauswein, A., Bastian, N.-U. F., Blaschke, D. B., Chatziioannou, K., Clark, J. A., Fischer, T., & Oertel, M. 2019, *Phys. Rev. Lett.*, *122*(6), 061102.

Bauswein, A., Just, O., Janka, H.-T., & Stergioulas, N. 2017, *Astrophys. J. Lett.*, *850*, L34.

Bhattacharyya, A., Ghosh, S. K., Hanauske, M., & Raha, S. 2005, *Phys. Rev. C*, *71*, 048801.

Bilous, A. V., Watts, A. L., Harding, A. K., et al. 2019, *ApJ*, *887*(1), L23.

Birkhoff, G. D. 1923, *Relativity and Modern Physics*, Harvard University Press (Cambridge, MA).

Bishop, N. T., & Rezzolla, L. 2016, *Extraction of Gravitational Waves in Numerical Relativity*, 19, Living Reviews in Relativity. https://doi.org/10.1007/s41114-016-0001-9.

Blacker, S., Bastian, N.-U. F., Bauswein, A., et al. 2020, *Phys. Rev. D*, *102*(12), 123023.

Blaschke, D., Ayriyan, A., Alvarez-Castillo, D. E., & Grigorian, H. 2020, *Universe*, *6*(6), 81.

Burgio, G. F., Drago, A., Pagliara, G., Schulze, H.-J., & Wei, J.-B. 2018, *Astrophys. J.*, *860*, 139.

Christian, J.-E., & Schaffner-Bielich, J. 2020, *ApJ*, *894*(1), L8.

Christian, J.-E., Zacchi, A., & Schaffner-Bielich, J. 2019, *Phys. Rev. D*, *99*(2), 023009.

Copeland, E. J., Kopp, M., Padilla, A., Saffin, P. M., & Skordis, C. 2019, *Phys. Rev. Lett*, *122*(6), 061301.

Creminelli, P., & Vernizzi, F. 2017, *Phys. Rev. Lett.*, *119*(25), 251302.

Cromartie, H. T., Fonseca, E., Ransom, S. M., et al. 2020, *Nat. Astron.*, *4*, 72.

De, S., Finstad, D., Lattimer, J. M., Brown, D. A., Berger, E., & Biwer, C. M. 2018, *Phys. Rev. Lett.*, *121*(9), 091102.

Demorest, P. B., Pennucci, T., Ransom, S. M., Roberts, M. S. E., & Hessels, J. W. T. 2010, *Nature*, *467*, 1081.

Einstein, A. 1914, *Sitzungsberichte der Königlich Preussischen Akademie der Wissenschaften (Berlin)*, 1030.

Einstein, A. 1915a, *Sitzungsberichte der Königlich Preussischen Akademie der Wissenschaften (Berlin)*, 778.

Einstein, A. 1915b, *Sitzungsberichte der Königlich Preussischen Akademie der Wissenschaften (Berlin)*, 844.

Einstein, A. 1918, Sitzungsberichte der Königlich Preussischen Akademie der Wissenschaften (Berlin), *1918*, 154–167.

Gazdzicki, M. 2004, *J. Phys.*, *G30*, S701.

Gazdzicki, M., & Gorenstein, M. I. 1999, *Acta Phys. Polon.*, *B30*, 2705.

Glendenning, N. K., & Kettner, C. 2000, *Astron. Astrophys.*, *353*, L9.

Glendenning, N. K., Pei, S., & Weber, F. 1997, *Phys. Rev. Lett.*, *79*(9), 1603.

Hanauske, M. 2003, GSI Annual Report, *96*.

Hanauske, M., Bovard, L., Most, E., et al. 2019, *Universe*, *5*(6), 156.

Hanauske, M., & Greiner, W. 2001, *Gen. Relativ. Gravit.*, *33*, 739.

Hanauske, M., Steinheimer, J., Bovard, L., et al. 2017, *J. Phys. Conf. Ser.*, *878*, 012031.

Hanauske, M., Steinheimer, J., Motornenko, A., et al. 2019, *Particles*, *2*(1), 44.

Hanauske, M., Takami, K., Bovard, L., Rezzolla, L., Font, J. A., Galeazzi, F., & Stöcker, H. 2017, *Phys. Rev. D*, *96*(4), 043004.

Hinderer, T. 2008, *Astrophys. J.*, *677*, 1216.

Hinderer, T., Lackey, B. D., Lang, R. N., & Read, J. S. 2010, *Phys. Rev. D*, *81*(12), 123016.

Jebsen, J. T. 1921, *Arkiv for Matematik, Astronomi Och Fysik*, *15*, 18.

Kerr, R. P. 1963, *Phys. Rev. Lett.*, *11*, 237.

Kiuchi, K., Kyutoku, K., Shibata, M., & Taniguchi, K. 2019, *Astrophys. J.*, *876*(2), L31.

Li, J. J., Sedrakian, A., & Alford, M. 2020, *Phys. Rev. D*, *101*(6), 063022.

LIGO Scientific Collaboration, Virgo Collaboration, Gamma-Ray Burst Monitor, F., & INTEGRAL 2017, *Astrophys. J. Lett.*, *848*(2), L13.

Löffler, F., Faber, J., Bentivegna, E., et al. 2012, *Class. Quantum Grav*, *29*(11), 115001.

Malik, T., Alam, N., Fortin, M., et al. 2018, *Phys. Rev. C*, *98*(3), 035804.

Margalit, B., & Metzger, B. 2017, Constraining the Maximum Mass of Neutron Stars From Multi-Messenger Observations of GW170817. (ArXiv e-print 1710.05938)

Martí, J. M., Ibáñez, J. M., & Miralles, J. A. 1991, *Phys. Rev. D*, *43*, 3794.

Miller, M. C., Chirenti, C., & Lamb, F. K. 2020, *Astrophys. J.*, *888*(1), 12.

Miller, M. C., Lamb, F. K., Dittmann, A. J., et al. 2019, *ApJ*, *887*(1), L24.

Mishustin, I. N., Hanauske, M., Bhattacharyya, A., Satarov, L. M., Stöcker, H., & Greiner, W. 2003a, *Phys. Lett. B*, *552*(1–2), 1.

Montaña, G., Tolós, L., Hanauske, M., & Rezzolla, L. 2019, *Phys. Rev. D*, *99*(10), 103009.

Most, E. R., Jens Papenfort, L., Dexheimer, V., Hanauske, M., Stoecker, H., & Rezzolla, L. 2020, *Eur. Phys. J. A*, *56*(2), 59.

Most, E. R., Papenfort, L. J., Dexheimer, V., Hanauske, M., Schramm, S., Stöcker, H., & Rezzolla, L. 2019, *Phys. Rev. Lett.*, *122*(6), 061101.

Most, E. R., Weih, L. R., Rezzolla, L., & Schaffner-Bielich, J. 2018, *Phys. Rev. Lett.*, *120*(26), 261103.

Oppenheimer, J. R., & Volkoff, G. 1939, *Phys. Rev.*, *55*, 374.

Paschalidis, V., Yagi, K., Alvarez-Castillo, D., Blaschke, D. B., & Sedrakian, A. 2018, *Phys. Rev. D*, *97*, 084038.

Penrose, R. 1965, *Phys. Rev. Lett.*, *14*, 57.

Postnikov, S., Prakash, M., & Lattimer, J. M. 2010, *Phys. Rev. D*, *82*(2), 024016.

Raaijmakers, G., Riley, T. E., Watts, A. L., et al. 2019, *ApJ*, *887*(1), L22.

Radice, D., Perego, A., Zappa, F., & Bernuzzi, S. 2018, *ApJ*, *852*(2), L29.

Radice, D., Rezzolla, L., & Galeazzi, F. 2014a, *Mon. Not. R. Astron. Soc. L.*, *437*, L46.

Radice, D., Rezzolla, L., & Galeazzi, F. 2014b, *Class. Quant. Grav.*, *31*(7), 075012.

Raithel, C., Özel, F., & Psaltis, D. 2018, *Astrophys. J.*, *857*, L23.

Rezzolla, L., Most, E. R., & Weih, L. R. 2018, *Astrophys. J. Lett.*, *852*, L25.

Rezzolla, L., & Zanotti, O. 2013, *Relativistic Hydrodynamics*, Oxford University Press (Oxford, UK).

Riley, T. E., Watts, A. L., Bogdanov, S., et al. 2019, *ApJ*, *887*(1), L21.

Ruiz, M., Shapiro, S. L., & Tsokaros, A. 2018, *Phys. Rev. D*, *97*(2), 021501.

Schwarzschild, K. 1916a, *Sitzungsber. Dtsch. Akad. Wiss. Berlin, Kl. Math. Phys. Tech.*, *1*, 424.

Schwarzschild, K. 1916b, *Sitzungsber. Dtsch. Akad. Wiss. Berlin Kl. Math. Phys. Tech.*, *1*, 189.

Shibata, M., Zhou, E., Kiuchi, K., & Fujibayashi, S. 2019, *Phys. Rev. D*, *100*(2), 023015.

Shovkovy, I., Hanauske, M., & Huang, M. 2003, *Phys. Rev. D*, *67*, 103004.

Tews, I., Carlson, J., Gandolfi, S., & Reddy, S. 2018, *Astrophys. J.*, *860*, 149.

The LIGO Scientific Collaboration, & the Virgo Collaboration 2016, *Phys. Rev. Lett*, *116*(6), 061102.

The LIGO Scientific Collaboration, & the Virgo Collaboration 2018, *Phys. Rev. Lett.*, *121*, 161101.

The LIGO Scientific Collaboration, & the Virgo Collaboration 2019a, *Phys. Rev. X*, *9*(3), 031040.

The LIGO Scientific Collaboration, & the Virgo Collaboration 2019b, *Phys. Rev. Lett.*, *123*(1), 011102.

The LIGO Scientific Collaboration, & the Virgo Collaboration 2020a, *ApJ*, *892*(1), L3.

The LIGO Scientific Collaboration, & the Virgo Collaboration 2020b, *Phys. Rev. Lett.*, *125*(10), 101102.

The LIGO Scientific Collaboration, & the Virgo Collaboration 2020c, *ApJ*, *896*(2), L44.

The LIGO Scientific Collaboration, & the Virgo Collaboration. 2020d, *arXiv e-prints*, arXiv:2010.14527.

The LIGO Scientific Collaboration, & the Virgo Collaboration. 2020e, *ApJ*, *900*(1), L13.

The LIGO Scientific Collaboration, the Virgo Collaboration, & the KAGRA Collaboration. 2020, *arXiv e-prints*, arXiv:2012.12926.

The LIGO Scientific Collaboration, the Virgo Collaboration, & the KAGRA Collaboration. 2021a, *arXiv e-prints*, arXiv:2101.12248.

The LIGO Scientific Collaboration, the Virgo Collaboration, & the KAGRA Collaboration. 2021b, *arXiv e-prints*, arXiv:2101.12130.

Tolman, R. C. 1939, *Phys. Rev.*, *55*, 364.

Tolos, L., Centelles, M., & Ramos, A. 2017a, *Astrophys. J.*, *834*, 3.

Tolos, L., Centelles, M., & Ramos, A. 2017b, *Publ. Astron. Soc. Austral.*, *34*, e065.

Troja, E., Piro, L., van Eerten, H., et al. 2017, *Nature*, *551*(7678), 71.

Weih, L. R., Hanauske, M., & Rezzolla, L. 2020, *Phys. Rev. Lett*, *124*(17), 171103.

Zhao, T., & Lattimer, J. M. 2018, *Phys. Rev. D*, *98*(6), 063020.

AUTHOR BIOGRAPHY

Matthias Hanauske studied physics at Frankfurt am Main and Konstanz; Diploma in physics at University Konstanz 1997, PhD in physics at University Frankfurt 2004, PhD in economics at University Frankfurt 2011, afterwards researcher and lecturer at University Frankfurt and Frankfurt Institute for Advanced Studies.